

Can CoGeNT and DAMA Modulations Be Due to Dark Matter?

Marco Farina^a, Duccio Pappadopulo^b,
Alessandro Strumia^{c,d}, Tomer Volansky^{e,f}

(a) *Scuola Normale Superiore and INFN, Piazza dei Cavalieri 7, 56126 Pisa, Italia*

(b) *Institut de Théorie des Phénomènes Physiques, EPFL, CH-1015 Lausanne, Switzerland*

(c) *Dipartimento di Fisica dell'Università di Pisa and INFN, Italia*

(d) *National Institute of Chemical Physics and Biophysics, Ravala 10, Tallinn, Estonia*

(e) *Berkeley Center for Theoretical Physics, Department of Physics,
University of California, Berkeley, CA 94720, USA*

(f) *Theoretical Physics Group, Lawrence Berkeley National Laboratory,
Berkeley, CA 94720, USA*

Abstract

We explore the dark matter interpretation of the anomalies claimed by the DAMA and CoGeNT experiments, in conjunction with the various null direct-detection experiments. An independent analysis of the CoGeNT data is employed and several experimental and astrophysical uncertainties are considered. Various phenomenological models are studied, including isospin violating interactions, momentum-dependent form factors, velocity-dependent form factors, inelastic scatterings (endothermic and exothermic) and channeling. We find that the severe tension between the anomalies and the null results can be ameliorated but not eliminated, unless extreme assumptions are made.

Contents

1	Introduction	2
2	Formalism	4
2.1	Dark Matter velocity distributions	5
3	Experiments	6
3.1	DAMA	6
3.2	CoGeNT	8
3.3	SIMPLE	10
3.4	XENON100	12
3.5	XENON10	13
3.6	CDMS-Si	14
3.7	CDMS-Ge	15
4	Results	15
4.1	Format of the figures	15
4.2	Standard fit	17
4.3	Astrophysical uncertainties	18
4.4	Quenching factor uncertainties in DAMA	19
4.5	Isospin violating couplings	19
4.6	Momentum-dependent elastic scattering	20
4.7	Velocity-dependent elastic scattering	22
4.8	Inelastic light Dark Matter scattering	23
4.9	Channeling	24
4.10	Channeling plus inelasticity	25
5	Conclusions	27

1 Introduction

Significant on-going efforts are being made to directly search for Weakly Interacting Massive Particles (WIMPs). An interesting and widely accepted signature of WIMPs is the annual modulation of their interaction rate, arising from the relative motion of the Earth around the Sun. Strikingly, both the DAMA [1] and CoGeNT [2, 3] collaborations observe anomalous modulating events that may be interpreted as arising from interactions of spin-independent Dark Matter (DM). As we discuss below, the two measurements are, to some extent, consistent with each other, and point to a surprisingly low DM mass, of order a few GeV.

In contrast to the positive signals of DAMA and CoGeNT, several other experiments find no evidence for DM. Most notably, the CDMS [4], XENON10 [5] and the XENON100 [6]

collaborations seem to disfavor the parameter space indicated by DAMA and CoGENT. It is natural to ask, therefore, what possible systematic effects and/or DM properties can resolve the tension between the positive and null results?

One noticeable difference between DAMA/CoGENT and the null experiments, is that the latter veto electronic interactions while attempting to collect only nuclear recoil events. It is conceivable that the anomalous signals arise from such electronic recoils, a possibility that would explain away the existing tension. A model of this type was considered in [7, 8] prior to the recent CoGENT measurement [3] and it remains to be seen whether this possibility is theoretically feasible. In this paper we pursue a different direction and study the viability of nuclear recoils of spin independent DM, as an explanation to the positive signals. Several handles can, in principle, ameliorate the tension with the null results. From the DM perspective one may consider,

- Inelastic scattering (endothermic or exothermic) [9, 10, 11].
- Isospin-violating couplings [12, 13, 14, 15, 16, 17, 18].
- Velocity suppressed interactions.
- Momentum dependent scattering [19, 20].
- Resonant scattering [21].

In addition there are uncertainties that may significantly change the expected scattering rates in various experiments:

- Astrophysical uncertainties [22, 23, 24, 25, 26, 27, 28, 29, 30].
- Possible channeling effects [31, 32] (see however [33]).
- Uncertainties in the Xenon scintillation function at low recoil energies or in the statistical treatment of the background events (for a discussion, see e.g. [34]).

A fully systematic analysis that takes into account all of the theoretical and experimental uncertainties above is hard to attain and we do not attempt here. Instead, we separately study the effects of most of the above possibilities on the DM interpretation of the DAMA and CoGENT results, as well as the null experiments.

Our goal is two-fold. Primarily, we aim at understanding to what extent the DAMA and CoGENT results are consistent with each other, and with the other null experiments (for related works, see [35]). In addition, we study what is required from the theoretical point of view and what needs to be assumed on the experimental side, in order to ameliorate the tension. Along the way, we reanalyze the CoGENT modulation data.

The paper is organized as follows. In Section 2 we summarize the standard computation of the expected signals and shortly discuss the DM velocity distributions considered here. In Section 3 we describe the experimental data we use, dwelling on the various uncertainties and

discussing their influence on the fits. Our results are presented in Section 4. Here we follow the analyses endorsed by the various experimental collaborations and explore whether velocity distributions or any of the DM scenarios mentioned above can explain the signals compatibly with the bounds. We conclude in section 5.

2 Formalism

The direct detection rate for DM–nucleus scattering at a given experiment is given by

$$\frac{dR}{dE_R} = N_T \frac{\rho_\odot}{M_{\text{DM}}} \int_{|\vec{v}| > v_{\text{min}}} d^3v v f_\oplus(v, t) \frac{d\sigma}{dE_R}, \quad (2.1)$$

where N_T is the number of target nuclei per unit mass of the detector, M_{DM} is the DM mass, ρ_\odot is the local DM density (that we assume to be equal to $0.3 \text{ GeV}/\text{cm}^3$) and $f_\oplus(v, t)$ is the DM velocity distribution in the Earth frame, to be discussed below. We denote σ to be the DM–nucleus scattering cross section, which we take to be of the form,

$$\frac{d\sigma}{dE_R} = \frac{m_N \sigma_n}{2v^2 \mu_n^2} \frac{[f_p Z + f_n (A - Z)]^2}{f_n^2} F_N^2(q) F_{\text{DM}}^2(q, v). \quad (2.2)$$

Here m_N is the nucleus mass, μ_n is the DM-nucleon reduced mass, f_p (f_n) is the coupling strength to the proton (neutron) and $F_N(q)$ is the nucleus form factor. Throughout this work we use the Helm form factor given in [36]. The DM form factor, $F_{\text{DM}}(q, v)$, is a velocity and/or momentum dependent contribution to the cross section which may exist, depending on the DM coupling. Below we consider several possibilities for its form. Finally, v_{min} appearing in Eq. (2.1) is the minimal DM velocity needed for a scattering with a recoil energy E_R to occur. In the elastic scattering case, it is given by

$$v_{\text{min}} = \sqrt{\frac{m_N E_R}{2\mu^2}}. \quad (2.3)$$

In Section 4.8 we consider inelastic scattering, in which case the required minimal velocity depends further on the mass splitting, $\delta = M'_{\text{DM}} - M_{\text{DM}}$, of the recoiling particles:

$$v_{\text{min}} = \frac{1}{\sqrt{2m_N E_R}} \left| \frac{m_N E_R}{\mu} + \delta \right|. \quad (2.4)$$

The scattering rate is expected to be time-dependent, exhibiting a maximum at the beginning of June (when the Earth moves against the DM wind) and a minimum at the beginning of December (when the Earth moves along the DM wind). It is thus useful to define a modulated rate as

$$\frac{dR_{\text{mod}}}{dE_R} = \frac{1}{2} \left[\frac{dR}{dE_R}(\text{2 June}) - \frac{dR}{dE_R}(\text{2 December}) \right]. \quad (2.5)$$

Both the modulated and unmodulated rates can be confronted with the results of an experiment only after accounting for all expected backgrounds and experimental efficiencies. The modulated rate is, in particular, independent of any time-independent background which can contaminate the DM signal.

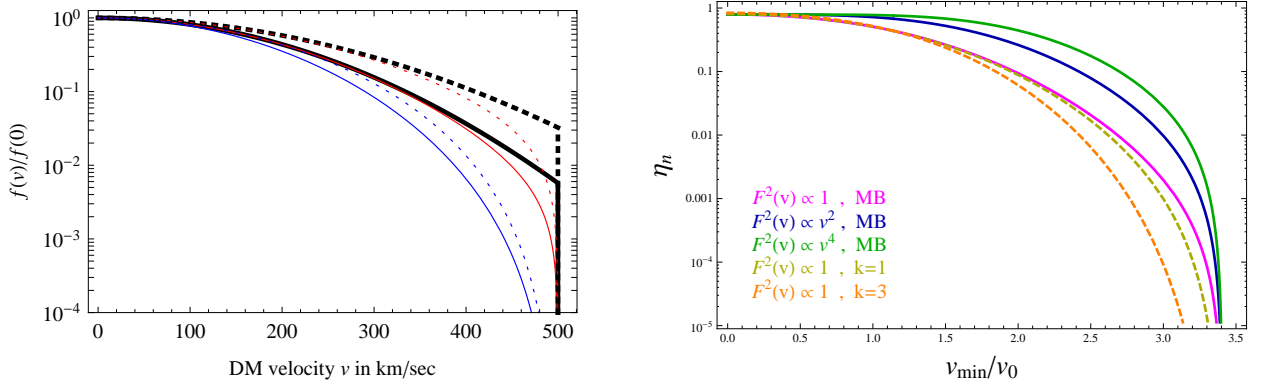


Figure 1: **Left:** Dark Matter velocity distributions: the Maxwell-Boltzmann with sharp cutoff at $v = v_{\text{esc}} = 500$ km/s (thick black curve), the distribution, Eq. (2.8), with a smooth cutoff computed for $k = 1$ (red) and $k = 3$ (blue). Two different values of v_0 are shown: 220 km/s (solid) and 270 km/s (dotted). **Right:** The function η_n defined in Eq. (2.9) as a function of the minimal DM velocity, v_{\min} , normalized to the mean DM velocity, v_0 . As discussed in the text, this function captures the effect of velocity-dependent form factor on the total scattering rate. We plot $F_{\text{DM}}^2(v) = 1, v^2/v_0^2, v^4/v_0^4$ (magenta, blue and green respectively) for the Maxwell-Boltzmann distribution. For completeness we also show the corresponding function for the \tilde{f}_k velocity distribution defined in Eq. (2.8) with a trivial form factor. $k = 1$ (dashed yellow) and $k = 3$ (dashed orange) are shown. For all lines, we use, $v_0 = 220$ km/sec, $v_{\text{esc}} = 500$ km/sec, and take the Earth velocity on June 2nd.

2.1 Dark Matter velocity distributions

The DM interaction rate with nuclei depend on the velocity distribution f_{\oplus} of DM as in eq. (2.1). Since this distribution has not been measured, it adds its own source of uncertainty to the DM interpretation of direct detection experiments. This topic has been extensively studied in the literature, where several possibilities such as streams or velocity substructure were considered [23, 27, 28, 29]. While a systematic study of astrophysics uncertainties and its prospects for ameliorating the experimental tension is beyond the scope of this paper, we consider few motivated distributions to demonstrate the possible variation in the fits. We stress that it is conceivable for significantly different conclusions to be drawn with the use of less conventional or more exotic possibilities, as was demonstrated prior to the new COGENT result in, e.g. [27].

The velocity distribution in our local frame, $f_{\oplus}(v, t)$ defined in Eq. (2.1), is conveniently expressed in terms of the velocity distribution in the galactic frame, $\tilde{f}(v)$, through

$$f_{\oplus}(v, t) = \tilde{f}(v + v_{\oplus}(t); v_0, v_{\text{esc}}). \quad (2.6)$$

Here v_{\oplus} is the relative motion of the Earth with respect to the galactic frame (see e.g. [28] for further details). v_0 is the root mean square velocity typically taken to be in the range,

$220 < v_0 < 270$ km/s, while v_{esc} is the escape velocity, in the range, $450 < v_{\text{esc}} < 650$ km/s [22]. Below, we consider $v_0 = (220, 270)$ km/s and $v_{\text{esc}} = (500, 600)$ km/s.

The DM velocity distribution in the galactic frame is often assumed to be a Maxwell-Boltzmann (MB) sharply cut off by a finite escape velocity,

$$\tilde{f}_{\text{MB}}(v; v_0, v_{\text{esc}}) = \frac{1}{N_E} e^{-v^2/v_0^2} \Theta(v_{\text{esc}} - v), \quad (2.7)$$

with $N_E = (\text{erf}(z) - 2z \exp(-z^2) \pi^{-1/2}) \pi^{3/2} v_0^3$ and $z = v_{\text{esc}}/v_0$. Above, we have explicitly denoted the dependence of the velocity distribution on v_0 and v_{esc} . The above MB distribution does not seem to capture the results of N -body simulations [24, 25, 37, 38]. An improved ansatz for an isotropic velocity distribution is given by

$$\tilde{f}_k(v; v_0, v_{\text{esc}}) \propto \left[\exp\left(\frac{v_{\text{esc}}^2 - v^2}{k v_0^2}\right) - 1 \right]^k \Theta(v_{\text{esc}} - v) \quad (2.8)$$

for $1.5 < k < 3.5$ [29]. The MB distribution is reobtained in the limit $k \rightarrow 0$. These velocity distributions are plotted in Fig. 1a.

The above distributions enter the scattering rate, Eq. (2.1), through the function,¹

$$\eta_n \left(\frac{v_{\text{min}}}{v_0}, \frac{v_{\oplus}}{v_0}, \frac{v_{\text{esc}}}{v_0} \right) = \int_{|\vec{v}| > v_{\text{min}}} d^3v f_{\oplus}(v, t) \left(\frac{v}{v_0} \right)^{-1} F_{\text{DM}}^2(q, v). \quad (2.9)$$

Note that the dependence on v_{\oplus} and v_{esc} is implicit through the definition of f_{\oplus} [see Eq. (2.6)]. In Fig. 1b we plot η_n for $F_{\text{DM}}^2(q, v) = 1, v^2/v_0^2, v^4/v_0^4$ with the Maxwell-Boltzmann distribution, as well as the trivial form factor for the \tilde{f}_k velocity distribution defined in Eq. (2.8). As can be seen, higher powers of velocity in the form factor imply a larger overall normalization and a larger sensitivity to higher minimal velocity with a sharper falloff. We return to these features in η_n in Section 4.7, where we study velocity-dependent form factors.

3 Experiments

In this section we briefly summarize the data used to derive the allowed region for spin-independent DM scattering. For each experiment we stress the various sources of uncertainties and our approach for dealing with them. In most cases, we consider several possibilities, allowing for a conservative view of the tension between the positive and null experimental results.

3.1 DAMA

The DAMA experiment employs a NaI(Tl) target and observes an 8.9σ evidence for an annual modulation in its energy spectrum [1]. The modulation is present in the 2-6 keVee energy range and the time dependence of the rate is consistent with the hypothesis of DM scattering

¹We use the notations of [28], however our function η_n is chosen to be dimensionless, as opposed to the corresponding function defined in [28].

bin (keVee)	rate (cpd ⁻¹ kg ⁻¹ keVee ⁻¹)	σ_{rate}
2–2.5	0.016	0.004
2.5–3	0.026	0.005
3–3.5	0.022	0.005
3.5–4	0.008	0.005
4–4.5	0.011	0.004
4.5–5	0.005	0.004
5–5.5	0.009	0.003
5.5–6	0.004	0.003
6–14	0.000	0.000

Table 1: *The data used in the fit to the DAMA modulated amplitude.*

on nuclei. The DAMA experiment is able to measure only the fraction of energy that recoil nuclei deposit as scintillation. This fraction of the total recoil energy, known as the quenching factor, is taken to be $q_{\text{I}} = 0.09$ for Iodine.

Different groups report varying values for the quenching factor on Sodium. The DAMA collaboration reports $q_{\text{Na}} = 0.30 \pm 0.01$ averaging over recoil energies ranging from 6.5 to 97 keV. Ref. [39] finds 0.33 ± 0.15 between 4 to 11 keV while ref. [40] finds 0.252 ± 0.065 around 10 keV. The relevance of q_{Na} resides in the fact that larger values ameliorate the apparent tension between DAMA and the null experiments. Indeed larger q_{Na} implies lower recoil energies at DAMA and consequently favors smaller WIMP masses. Following many previous works, we adopt a conservative estimation of the uncertainties, assuming $q_{\text{Na}} = 0.3 \pm 0.1$.

An additional source of uncertainty arises due to the crystalline nature of the target material. It is possible that some (experimentally unknown) fraction of the ion scatterings occur parallel to a symmetry axis (channeled events), depositing the entire energy in scintillation. For such events the quenching factor is effectively 1 and hence a sizable fraction of channelled events may significantly alter the direct detection predictions [31]. Recent theoretical results, suggest that the channeling fraction in NaI is negligible [33]. In order to be *over-conservative*, in Section 4.9 we also perform fits in which we allow an energy independent channeling fraction.

The spin independent fit to the DAMA modulated rate allows two qualitatively different best-fit regions: one around $M_{\text{DM}} \approx 80$ GeV with $\sigma \approx 10^{-41}$ cm² due to scattering on iodine ($A = 127$, $Z = 53$) and one around $M_{\text{DM}} \approx 10$ GeV with $\sigma \approx 10^{-40}$ cm² due to scattering on sodium ($A = 23$, $Z = 11$). The former region is firmly excluded by many other experiments, most notably XENON10/100. The latter region, while still disfavored by other null searches, is not as badly excluded due to many experimental uncertainties and due to the general difficulty of direct detection searches to deal with low recoil energy scatterings. In the following we will focus on this low mass region, being also the only possibility to reconcile DAMA with the results of CoGENT.

	N	$\delta N/N$	E_{peak} (keV)	$\sigma_{E_{\text{peak}}}$	$T_{1/2}$ (days)
^{73}As	12.7	0.33	1.414	0.078	80
^{68}Ge	639	0.01	1.298	0.077	271
^{68}As	52.8	0.05	1.194	0.076	271
^{65}Zn	211	0.02	1.096	0.076	244
^{56}Ni	1.53	0.23	0.926	0.075	6
$^{56,58}\text{Co}$	9.44	0.45	0.846	0.074	71
^{57}Co	2.59	3.81	0.846	0.074	271
^{55}Fe	44.9	0.12	0.769	0.074	996
^{54}Mn	21.1	0.09	0.695	0.074	312
^{51}Cr	2.94	0.15	0.628	0.073	28
^{49}V	14.9	0.12	0.564	0.073	330

Table 2: *The data used to extract the L-shell backgrounds. N is the total number of decays expected from a given isotope from the beginning of the CoGENT data taking to the end of time, with $\delta N/N$ being its relative error. E_{peak} is the central value for the corresponding binding energy while $\sigma_{E_{\text{peak}}}$ is the energy resolution. $T_{1/2}$ is the half-life of the relevant isotope.*

To fit the modulated signal at DAMA we build a simple χ^2 using the content of the first 8 bins in Fig. 9 of [1]. We use a single bin for the modulated rate in the energy range of 6 to 14 keVee. The data we use are shown in Table 1. DAMA collaboration also reports (see fig. 1 of [41]) a measurement of its non-modulated rate. This can be used to define an upper bound on the signal, following for instance the procedure of [42]. Unless stated otherwise, we will not use this bound in the fits.

To compare the data with the theoretical hypothesis we introduce a finite detector resolution, parameterizing the energy smearing through a gaussian with energy dependent width given by,

$$\sigma_{\text{DAMA}} \left(\frac{E}{\text{keVee}} \right) = 0.448 \sqrt{\frac{E}{\text{keVee}}} + 9.1 \times 10^{-3} \frac{E}{\text{keVee}}. \quad (3.1)$$

3.2 CoGeNT

The CoGENT experiment uses a Germanium ($A \approx 76$, $Z = 32$) detector and takes data in the Soudan Underground Laboratory (SUL). We employ the latest data release [3], which are the result of 442 live days of data-taking from January 4 2010 to March 6 2011 on a 0.33 kg Germanium target. The new data confirm the presence of an exponential distribution of events between 0.5 and 1.5 keV which is not accounted for by any known background. A time analysis of the same data also shows evidence of an annual modulation in the 0.5–3.0 keV range, which could be interpreted as evidence for DM interacting with the detector.

To extract the rate and the modulation to be used in the fit, we use the time-stamped raw data obtained from the CoGENT collaboration [43]. The relevant region between 0.4 and

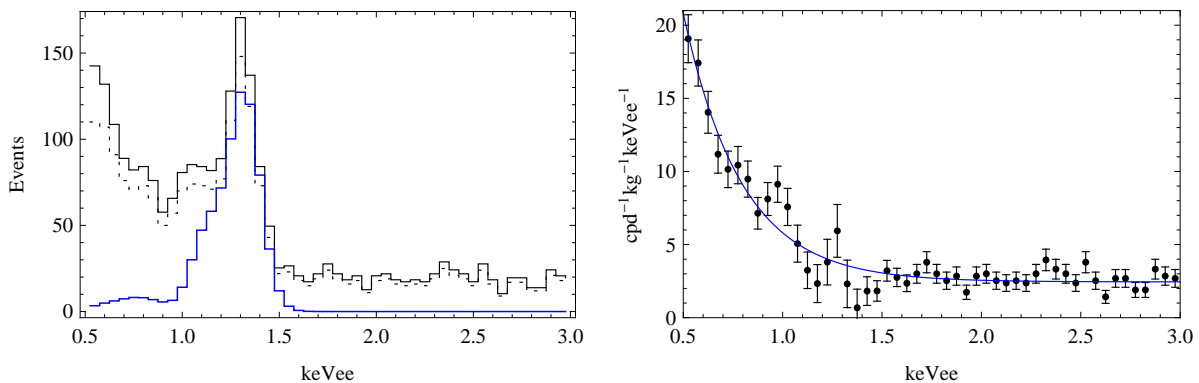


Figure 2: **Left:** *distribution of the events observed during 442 days of live-data taking (black dashed). The black line is the result of efficiency unfolding. The blue contour shows the contribution from L-shell EC lines calculated from the data in tab. 2.* **Right:** *COGENT non-modulated rate after the subtraction of L-shell lines. The blue line is the result of an exponential+constant fit to the rate. In both plots we use a uniform (0.1 keVee) binning.*

3.5 keV is contaminated by events due to the electron capture (EC) decay of cosmogenically activated elements in the detector. In a given time window these events are expected to show up as peaks centered around the L-shell binding energy of the daughter of the decaying nucleus. The width of the peaks is related to the detector resolution and its amplitude to the number of active isotopes in the detector. The amplitude of the peak is thus expected to decay in time with the half-life of the relative isotope. In Table 2 we show the parameters needed to describe these background events. It is clear that due to the time dependence of such backgrounds, their subtraction is of primary importance before attempting any time-analysis of the signal.

In Fig. 2 we show the spectrum of events observed at COGENT as well as the rate after efficiency unfolding. As shown, the residual events after subtracting the L-shell peaks, are well fitted by an exponential plus constant function $Ae^{-BE} + C$, with E in keVee. We find,

$$A = 100.4, \quad B = 3.4, \quad C = 2.4, \quad \chi^2/\text{d.o.f.} = 57/(50 - 3). \quad (3.2)$$

For the time-analysis we use data up to 6 keVee binned into 5 energy bins: 0.5-1, 1-2, 2-3, 3-4.5, 4.5-6 keVee. Each bin is further divided into 15 time bins of 30 days each. For every energy-time bin we subtract the estimated number of events from L-shell EC and apply a correction to account for the offline time. Since in the first bin the efficiency is not constant, we choose not to unfold it to avoid losing more statistics. A first test to the DM hypothesis is to check whether the signal modulates with a yearly period peaking on 2nd of June. We thus fit the signal to the function

$$\mathcal{B} + \mathcal{S} \cos \frac{2\pi(t - \phi)}{T}, \quad (3.3)$$

and check the consistency with the hypothesis $T = 365$ days and $\phi = 152$ days with the use of a χ^2 analysis, marginalizing over \mathcal{B} and \mathcal{S} . The results of the fit are shown in Fig. 3. The data

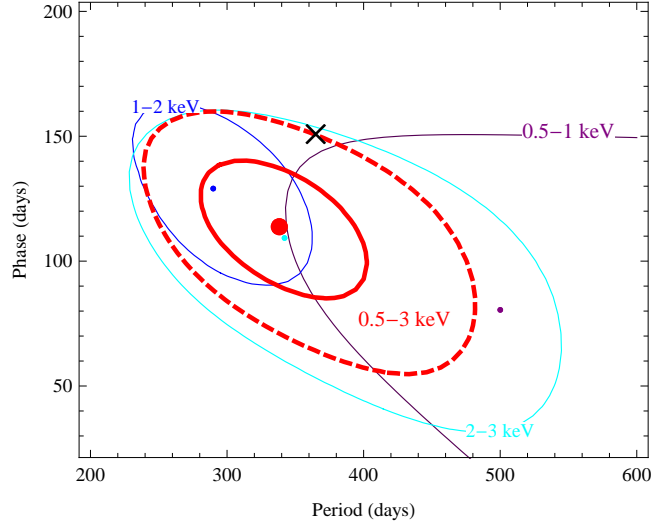


Figure 3: *Best fit for the period T and phase ϕ of the COGENT signal in the low energy bins. The continuous lines are the 1σ contours. For the large 0.5-3 keVee bin, we also show the 2σ one (dashed). The black cross indicates the prediction of the DM hypothesis.*

show consistency with the DM hypothesis at the 2σ level. The signal deviates from the null (no-modulation) hypothesis, at the 2σ level at most for each bin separately, while it exceeds this value (however not reaching 3-sigma) for the combined 0.5-3 keVee bin. The deviation from the null hypothesis is demonstrated further in Fig. 5, where the modulation spectrum is shown.

We thus fix T to the value predicted by the DM hypothesis, 365 days, and proceed to determine the best fit to the other parameters \mathcal{B} , \mathcal{S} and ϕ . The results are summarized in Table 3 and shown in Fig. 4. The dashed curves in Fig. 4 are obtained by fixing both $T = 365$ days and $\phi = 152$ days. To extract the amplitude of the modulation \mathcal{S} to be used in what follows, we marginalize over \mathcal{B} to obtain the spectrum shown in Fig. 5. In the two bins 0.5 – 3 and 3 – 6 keVee we get (in $\text{cpd}^{-1}\text{kg}^{-1}\text{keVee}^{-1}$)

$$0.5 - 3 \text{ keVee} : 0.43 \pm 0.18, \quad 3 - 6 \text{ keVee} : 0.02 \pm 0.11 \quad (3.4)$$

Finally, we need to specify the quenching factor of Germanium in order to translate keVee energy into keV nuclear recoil energies. We use a Lindhard $k = 2$ parametrization

$$\frac{E}{\text{keVee}} = 0.2 \left(\frac{E_R}{\text{keV}} \right)^{1.12}. \quad (3.5)$$

3.3 SIMPLE

The SIMPLE experiment is a superheated liquid C_2ClF_5 droplet detector. Working in a manner similar to bubble chambers it looks for bubble nucleations induced by WIMPs. In particular, due to the presence of light ions such as fluorine ($A = 19$, $Z = 9$), it is sensitive to light

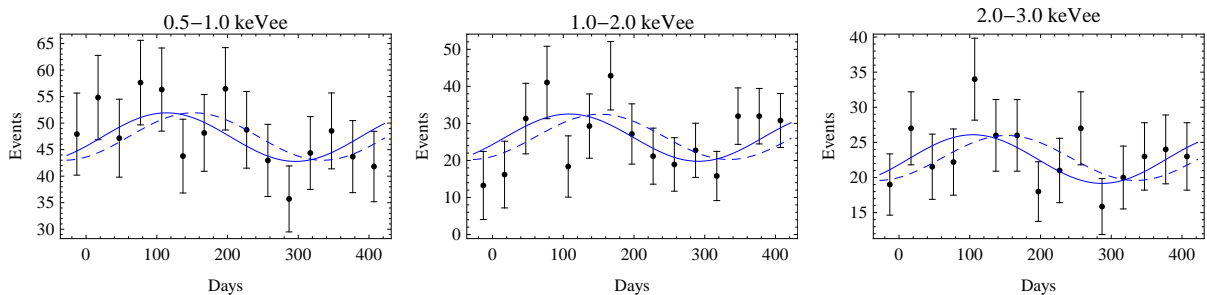


Figure 4: *Time-analysis of the data in the bins of interest. In all the fits we keep $T = 365$ days fixed. The blue full lines are obtained floating \mathcal{B} , \mathcal{S} and ϕ . The blue dashed lines are the results of the fit fixing also $\phi = 152$ days.*

E (keV)	\mathcal{B}	\mathcal{S}	ϕ	χ^2
0.5 – 1.0	47.3(47.6)	4.6(3.4)	114(152)	7.9(9.1)
1.0 – 2.0	26.1(26.3)	6.4(4.3)	108(152)	11.5(13.7)
2.0 – 3.0	22.6(22.8)	3.5 (2.1)	104(152)	8.0(10.1)
3.0 – 4.5	34.2(34.2)	0.2(0.1)	211(152)	15.7(15.7)
4.5 – 6.0	46.9(47.0)	1.9(0.3)	77(152)	21.2(21.7)
0.5 – 3.0	97.2(97.7)	15.0(10.7)	112(152)	6.3(11.0)
3.0 – 6.0	82.5(82.7)	2.7(0.7)	81(152)	14.3(14.9)

Table 3: *Summary of the time-analysis of the COGENT data. Everywhere $T = 365$ is fixed. The numbers in parenthesis are obtained fixing $\phi = 152$ days. The number of d.o.f. are 12 (13), in each energy bin.*

mass WIMPs even with a relatively high threshold of 8 keV. Although it is not possible for this kind of experimental setup to measure events' energies, the threshold can be set precisely as the bubble nucleation depends on the temperature and pressure of the superheated liquid. Neutron induced recoils has confirmed the minimum threshold energy at 8 keV with a precision of 0.1 keV.

The SIMPLE collaboration has recently published new results [44] including new Stage 2 data which improves and merges the analysis of older (Stage 1) data. As the merging can potentially introduce additional systematic uncertainties, we use only the Stage 2 data, with zero unidentified events and an exposure of 6.71 kg days. We set an exclusion limit using a Poissonian likelihood

$$\mathcal{L}_{\text{SIMPLE}} = e^{-N_{\text{DM}}}. \quad (3.6)$$

Such a likelihood is considered to be a conservative choice that produces bounds compatible with the official one.

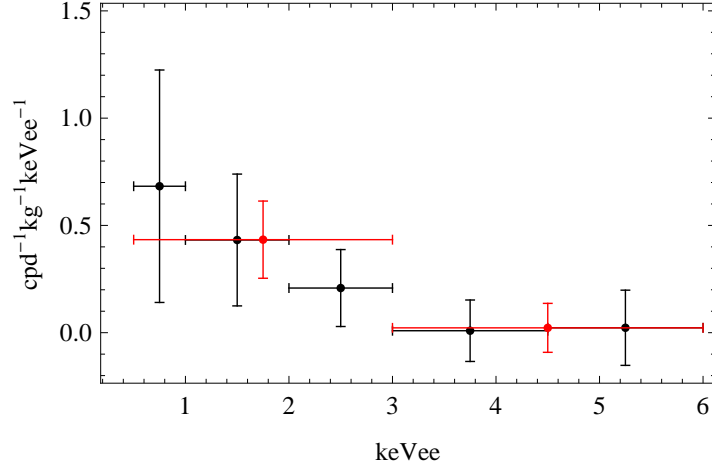


Figure 5: *Spectrum of the modulation amplitude in the COGENT data assuming $T = 365$ days and $\phi = 152$ days. In red we show the result of fitting just two bins: 0.5-3 and 3-6 keVee. No efficiency correction is applied.*

3.4 XENON100

XENON100 is a two-phase Xenon ($A \approx 131$, $Z = 54$) experiment which published results obtained from approximately 100 live days of data acquisition in a fiducial volume of 48 kg. The consistency of the outcome with the background hypothesis allows to place strong constraint on the interaction of a WIMP with Xenon nuclei.

As opposed to DAMA and COGENT, XENON100 has a signal-to-background discrimination ability. This is achieved by comparing the primary scintillation signal (S1) to the ionization yield (S2), the relative magnitude of the latter being bigger for electronic recoils. The capability of XENON100 to detect low mass WIMP scatterings crucially depends on the response function \mathcal{L}_{eff} which, through the relation

$$S1(E_R) = 3.6 \text{ PE} \times E_R \times \mathcal{L}_{\text{eff}}, \quad (3.7)$$

gives the number of photoelectrons (PE) in the S1 signal as a function of the recoil energy. Measurements of \mathcal{L}_{eff} extend down to 3 keV [45] while extrapolation have to be used for lower values. It was argued in [34], that the uncertainty on \mathcal{L}_{eff} significantly influences the ability of XENON100 to constrain light DM. Below, we use the \mathcal{L}_{eff} contours adopted by the XENON100 collaboration and shown in Fig. 1 of [6]. To have a good signal-to-background discrimination, the lower XENON100 threshold is fixed at 4 photoelectrons which corresponds to roughly 8 keV (depending on the precise choice of \mathcal{L}_{eff}). The relevance of the extrapolation of \mathcal{L}_{eff} to lower energies has to do with the statistical nature of the scintillation process. Assuming the photo-electron generation process to be poissonian in nature, with a mean dictated by Eq. (3.7), recoil occurring below threshold will have a non vanishing probability to generate an S1 signal above threshold. This tail is crucial to the constraining power of XENON100 for low mass WIMPs².

²The XENON100 analysis considers an S2 threshold of 300 photoelectrons. Values of $\langle S1 \rangle$ below threshold

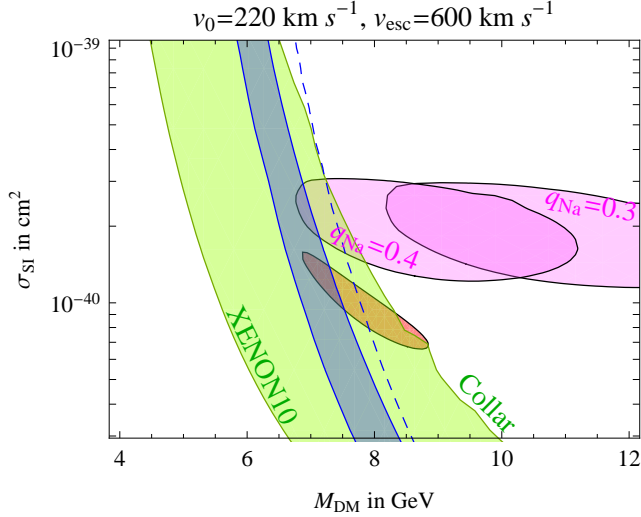


Figure 6: XENON100/10 bound compared with the 3σ favored region for DAMA (magenta) and COGENT (red). The blue band is the XENON100 exclusion obtained by varying \mathcal{L}_{eff} in its 1σ range. The blue dashed line shows the result of the conservative choice $\mathcal{L}_{\text{eff}} = 0$ below 4 keV. The light-green band represents how the 3σ XENON10 exclusion changes with respect to \mathcal{Q}_y variations: on the left we use the choice of the XENON10 collaboration and on the right we use the conservative estimate adopted in [34]. Two choices for the sodium quenching factor q_{Na} are adopted for the DAMA fits.

We have checked and found that assuming a different statistical behaviour of the S1-generation process (binomial for instance, see [34]) does not alter our conclusions. We show the XENON100 bound and its uncertainty in Fig. 6. The blue band is the 3σ exclusion obtained by varying \mathcal{L}_{eff} in its 1σ range [6]. The blue dashed line comes from the conservative choice of having $\mathcal{L}_{\text{eff}} = 0$ below 4 keV.

To determine the XENON100 bounds we follow [47] doing an event-by-event fit to the three observed events at energies 6, 19 and 22 keV assuming a uniform background in the region $4\text{ PE} \leq S1 \leq 30\text{ PE}$ normalized to the total number of expected events, 1.8. We include finite resolution effects through a gaussian smearing of the S1 signal with a width given by $0.5\sqrt{S1}$. We include an S1 peak finding efficiency in the same way it is done in [46]. We find this to be a small correction.

3.5 XENON10

The high XENON100 (XENON10) threshold, roughly 8 keV (5 keV), is related to the fact that recoils of too small energy are not efficiently converted into a primary scintillation signal S1. It is through comparison of this signal to the secondary scintillation (S2 signal) that the background from electronic recoil is subtracted.

may generate, through a statistical fluctuation, an S1 signal above threshold but may fail to pass the S2 cut. Following [46] we ignore recoils giving $\langle S1 \rangle \leq 1\text{ PE}$.

A low threshold analysis (1 keV) of XENON10 data is available [48] by discarding the S1 signal altogether and looking just at the S2 signal. Backgrounds are thus allowed to pollute the data but the gain in sensitivity at lower masses is substantial.

Since at low recoil energies the scintillation photons do not give a measurable S1 signal, one is forced to calibrate the energy scale using just the S2 signal. This calibration is encoded in the so called \mathcal{Q}_y parameter defined as

$$\mathcal{Q}_y(E_R) \equiv \frac{N_e(E_R)}{E_R}, \quad (3.8)$$

where N_e is the number of measured photoelectrons for a recoil of a given energy E_R . The role of \mathcal{Q}_y is similar to the one of \mathcal{L}_{eff} . Fixing a lower threshold for the magnitude of the S2 signal will, depending on \mathcal{Q}_y , define a lower threshold on the nuclear recoil energies probed by the experiment: the smaller the \mathcal{Q}_y the higher the effective threshold. Since the value of \mathcal{Q}_y is not measured below 4 keV [49, 50] extrapolations must be used.

XENON10 takes its S2 threshold at 5 photoelectrons, corresponding to roughly 1.4 keV with their choice of \mathcal{Q}_y . According to [34] this choice is far too generous. [34] thus proposes a smaller \mathcal{Q}_y (see details in the original reference) corresponding to an energy threshold of roughly 4 keV.

To calculate the XENON10 bounds we use the observed events in Fig. 3 of [48], corresponding to 15 kg days of effective exposure, passing all the 5 cuts detailed in Tab. 1 therein. In a fashion which resemble the p_{max} method [51], we determine the two consecutive events between which the total expected signal from DM is maximized. We use poissonian statistic to define the likelihood,

$$\mathcal{L}_{\text{Xe10}} = e^{-S_{2\text{DM}}}, \quad (3.9)$$

where S2 is the number of photoelectrons (including acceptances and poissonian statistical fluctuation which affects the S2 resolution) expected in the above interval under the DM hypothesis. We thus use $\chi^2_{\text{Xe10}} = -2 \ln \mathcal{L}_{\text{Xe10}}$ to set bounds. In the rest of the paper our choice for \mathcal{Q}_y is the same as the one adopted by the XENON10 collaboration. A comparison with the more conservative choice of [34] is shown in Fig. 6.

3.6 CDMS-Si

The cryogenic CDMS experiment (performed at the SUL like CDMS) operates Silicon ($A \approx 28$, $Z = 14$) and Germanium solid-state detectors. Like XENON100, CDMS has the ability to discriminate between nuclear recoils and electronic backgrounds, measuring both ionization and phonon signals. We use the results from the unofficial analysis [52, 53] of 6 Si detectors corresponding to a raw exposure of 53.5 kg.d. We use the efficiency reported in [52, 53] which drop to zero below 7.8 keV. No events are observed with an expectation of 1.1 events from surface backgrounds. We use the poissonian likelihood,

$$\mathcal{L}_{\text{Si}} = e^{-N_{\text{DM}}}, \quad (3.10)$$

where N_{DM} is the expected number of events under the DM hypothesis to extract the bounds.

As noted in [54], CDMS-Si data indicate a behavior for the Silicon quenching factor which is not in accord with the prediction of Lindhard theory (see for instance Fig. 3.20 of [52]). This can be ameliorated by correcting the energy scale by $\mathcal{O}(20\%)$, which also goes in the direction of weakening the CDMS-Si bounds but we do not include this correction in the fits.

3.7 CDMS-Ge

For the analysis of CDMS Germanium we employ the data obtained in the recent low-energy analysis [55], with an energy threshold of 2 keV. Since the electronic and the nuclear recoil bands merge at these low energies, the sensitivity to low WIMP masses offered by this low-threshold analysis comes at the price of accepting a large amount of background. Though the CDMS collaboration provides possible explanations for the background and claims that it can explain all the events in the signal region, they neglect it as being dependent on extrapolation and on too many uncertainties. This approach has been recently criticized in various ways [56]. In our analysis we follow the approach held by the CDMS collaboration not including backgrounds and treating, conservatively, all observed events as DM induced recoils. We depart, for simplicity, from the CDMS group retaining only the data coming from the best performing detector (T1Z5), that observed 36 events between 2 and 20 keV. By considering all the events as signal we construct a χ^2 by fitting the theoretical total rate N_{DM} , so that

$$\chi_{\text{Ge}}^2 = \frac{(N_{\text{DM}} - 36)^2}{36} \Theta(N_{\text{DM}} - 36). \quad (3.11)$$

Our bound agrees with the one reported by the CDMS collaboration. Due to the large number of observed events (and in the absence of background subtraction), the χ^2 function in Eq. (3.11) is rapidly growing thus giving confidence levels which are much closer to each other in comparison to the other experiments. This causes a deterioration of the global fit once the CDMS-Ge bound is included.

4 Results

In this section we present the best fit results for the experiments discussed above. Our approach here is to study the influence of different forms of cross-sections and velocity distributions, as discussed in the introduction, on the fits to the data. This approach differs somewhat from the usual effective theory one, where the bounds on different operators are studied. The virtue of the current method is that it allows one to identify the physical necessities in order to minimize the experimental tension. Realistic scenarios of course, often require taking linear combinations in either approaches.

4.1 Format of the figures

In our figures, all continuous (dotted) curves correspond to 95% (99.7%) C.L. for two degrees of freedom, i.e. 2σ (3σ) corresponding to $\Delta\chi^2 = 6$ ($\Delta\chi^2 = 11.6$). In the figures we show the

following:

- In purple, the region favored by the modulation observed by DAMA at fixed value of q_{Na} . The parameter fixed by the fit is essentially $M_{\text{DM}} \times q_{\text{Na}}$, such that considering a higher q_{Na} value shifts the favored region to lower DM masses. The text ‘DAMA’ lies over the DAMA best fit point.
- In yellow, the wide region favored by the modulation observed by CoGENT. We further impose that the DM rate alone does not exceed the rate observed by CoGENT in any point. In view of the poor statistical significance, we plot here the 68% C.L. contour (dashed-dotted) as well as the 95% C.L. contour.
- In red, the favored region for the rate observed by CoGENT (data in the right panel of fig. 2) assuming, in addition to the DM signal, an energy-independent constant term with normalization fixed as in Eq. (3.2). This assumes, arbitrarily, that the L-shell decays of activated isotopes account for the majority of low energy background events. The region favored by the CoGENT rate up to this caveat is shown in red and marked as ‘CR’.
- A green curve for the bound obtained with the CDMS Silicon result, denoted as ‘Si’.
- A red curve for the bound by CDMS with Germanium, denoted as ‘Ge’.
- A blue curve for the bound by XENON100, denoted as ‘Xe₁₀₀’.
- A purple curve for the bound by XENON10, denoted as ‘Xe₁₀’.
- A dark yellow curve for the bound from SIMPLE, denoted as ‘C Cl F’.
- Finally, we plot a green dot indicating the global best fit taking into account all signals and bounds.

We define the global χ^2 as $\chi^2 = \sum_i \chi_i^2$, summing over all the relevant experiments, and report the value of χ^2 for the best fit point. Such χ^2 can be used as statistical indicator to compare different fits and to evaluate the overall quality of the fit (although other more sensitive statistical indicators exist). For experiments that give bounds we fixed $\chi_i^2 = 0$ when no DM is present, such that we expect that a good fit should correspond to $\chi^2 \sim n_{\text{obs}} - n_{\text{par}}$, where n_{obs} is the number of observed data-points and n_{par} the number of free parameters. Since the CoGENT rate could be contaminated by unknown backgrounds at low energy, we perform two global fits:

- Fitting all data including the CoGENT rate. A good fit should have $\chi_{\text{ij}}^2 \sim 43$, as we fit 35 data points in the CoGENT rate, 9 in the DAMA modulation, 2 in the CoGENT modulation with a number of free parameters going from 2 to 4;
- Fitting all data (the CoGENT modulation and all other experiments) but dropping the CoGENT rate. A good fit should have $\chi_{\text{ii}}^2 \sim 8$.

In the pictures we report the value of both χ^2 evaluated at their best-fits, using the format “ $\chi^2 = \chi_{\text{ij}}^2, \chi_{\text{ii}}^2$ ”. Our Results are presented in the next sub-sections.

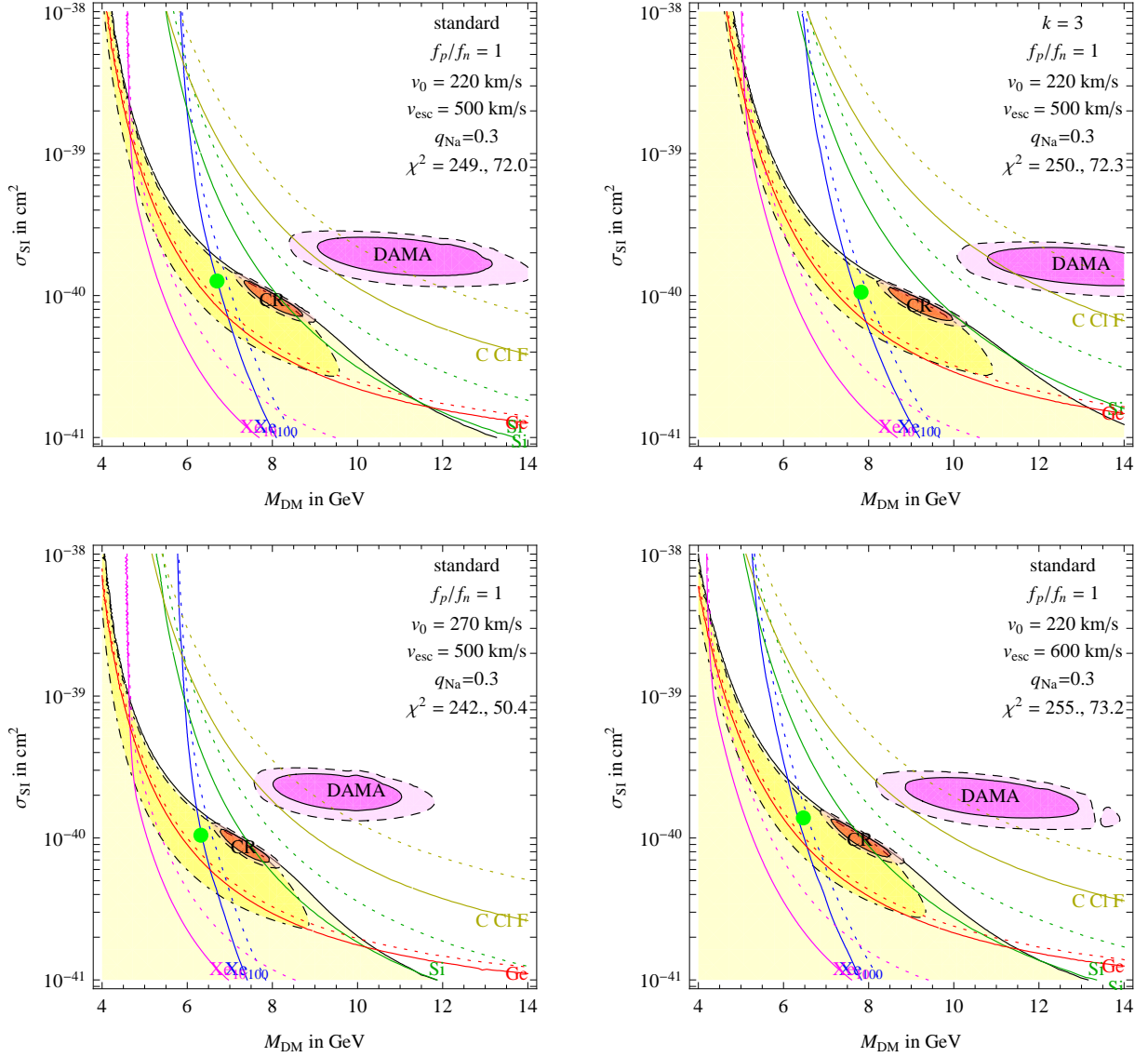


Figure 7: **Upper left:** *Standard fit.* DAMA and COGENT do not overlap, and are excluded by many experiments. In the other plots we vary the DM velocity distribution, finding minor changes. On the **top right:** we use the smooth distribution of Eq. (2.8) with $k = 3$. **Bottom left** A higher $v_0 = 270$ km/s and lower $v_{esc} = 500$ km/s are assumed. **Bottom right:** A higher $v_{esc} = 600$ km/s is taken. In all plots $f_p/f_n = 1$ and $q_{Na} = 0.3$. See Section 4.1 for the color coding.

4.2 Standard fit

In Fig. 7a we show the “standard” fit, in terms of elastic spin-independent DM, using the cross-section in Eq. (2.2), and assuming no form factor, $F_{DM} = 1$ and $f_n = f_p = 1$. We see that (i) DAMA and COGENT do not overlap and (ii) they are excluded or strongly disfavored by many experiments. As a result the global best fit (green dot) has a very high χ^2 , and corresponds to roughly no effect in DAMA.

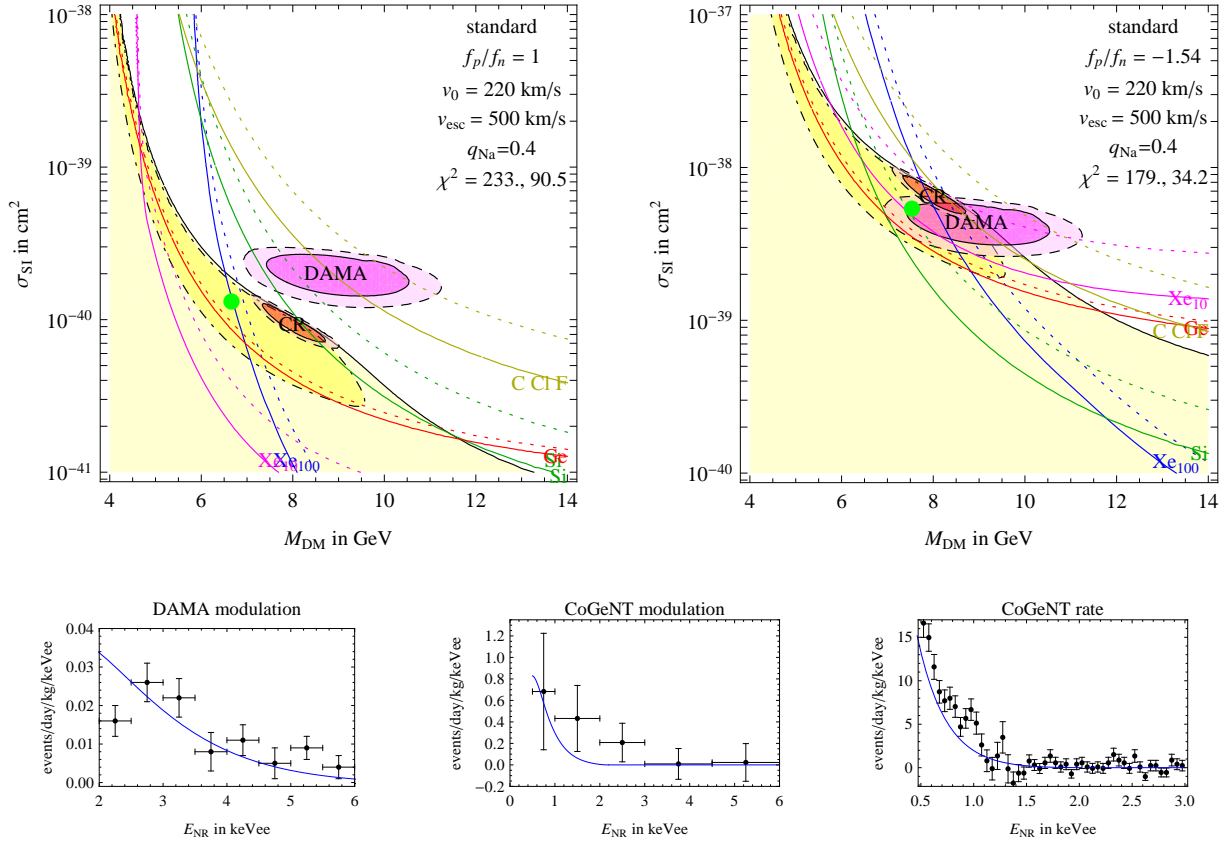


Figure 8: **Top left:** Standard fit assuming a higher quenching factor for Sodium, $q_{\text{Na}} = 0.4$. **Top right:** Global fit assuming isospin-violation, dictated by the f_p/f_n parameter. The situation significantly improves, but the best fit (marked with a green dot) remains very poor. Color coding is described in Section 4.1. **Bottom:** DM predictions for the best fit point, allowing a floating f_p/f_n . The signal is plotted against the DAMA and CoGeNT modulated and unmodulated data.

4.3 Astrophysical uncertainties

We explore the sensitivity to modifications in the velocity distributions (under the assumption of isotropy) by first considering the smoothed cuts discussed in section 2.1, as controlled by the parameter k : bigger k implies a smoother distribution while the sharply cut, Maxwell Boltzmann distribution is obtained in the $k \rightarrow 0$ limit. These velocity distributions are shown in Fig. 1a. As can be seen in Fig. 7b the fits to the experimental data assuming a DM velocity distribution with a smooth $k = 3$ cut are quite similar to the ones for $k \rightarrow 0$ (Fig. 7a). In view of the very minor difference from now on we stick to sharp cuts and we do not show the intermediate case $k = 1$.

The improvement in changing v_0 is also small. The slope of DAMA (CoGeNT) spectrum fixes the value of $\mu^2 v_0^2 / m_N$, hence for low-mass WIMPs raising v_0 favors smaller DM masses. The effects are shown in Fig. 7c. Similarly, changing the maximal DM velocity v_{esc} does not

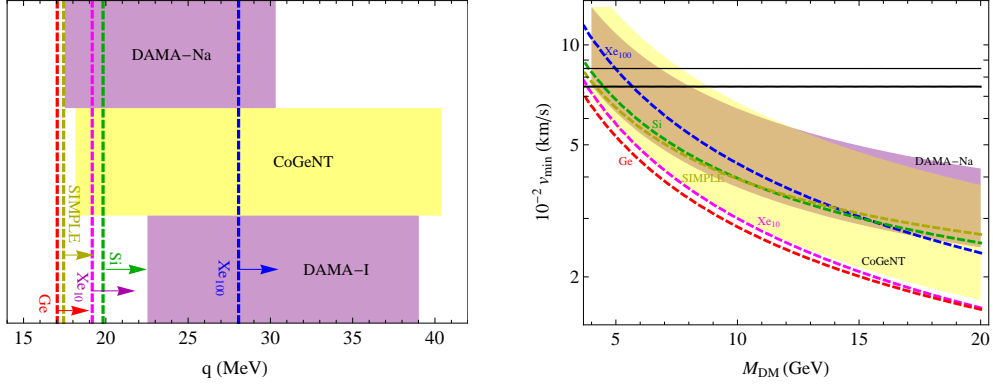


Figure 9: *Ranges of transferred momentum q (left) and minimal DM velocities, v_{\min} , (right) probed by relevant experiments. Solid bands: COGENT 0.5-3.0 keVee band (yellow) and DAMA 2-6 keVee bands (purple) for both unchanneled Sodium (upper panel) and channeled Iodine (lower panel). Dashed lines: XENON100 3 keV threshold (blue), CDMS-Si 7 keV threshold (green), CDMS-Ge 2 keV threshold (red) and SIMPLE 8 keV threshold (dark yellow). The horizontal lines show the maximum possible DM velocity in the Earth frame for $v_{\text{esc}} = 500$ km/s (thick) and $v_{\text{esc}} = 600$ km/s (thin).*

help, see Fig. 7d.

4.4 Quenching factor uncertainties in DAMA

Assuming a quenching factor for Na higher than what is claimed by the DAMA collaboration, allows to shift the DAMA best fit region to lower M_{DM} (the combination $M_{\text{DM}} \times q_{\text{Na}}$ being essentially fixed), improving the fit. In Fig. 8a we show the case $q_{\text{Na}} = 0.4$, that we will adopt from now on. Even so, the best fit is so bad that we do not show its comparison with data.

4.5 Isospin violating couplings

It is possible that DM does not couple equally to protons and neutrons. Such isospin-violating DM scattering has been studied against the COGENT rate data previously in [15, 16, 17]. In Fig. 8b (and in the rest of the fits) we relax the assumption of $f_p = f_n$, and allow for different spin-independent cross sections on protons and neutrons. As can be seen, floating the additional parameter, f_p/f_n , allows to

- Improve the agreement between COGENT and DAMA.
- Ameliorate the tension of the positive results with one experimental bound, through the tuning of $f_p Z + f_n(A - Z) \approx 0$. In our fits, we take into account the different isotopes in the various experiments, thereby allowing for only a partial cancelation.

When performing a global fit, we find the best-fit shown in Fig. 8b, with a significant improvement over the $f_p = f_n$ case shown in Fig. 8a. Still, the global fit remains very poor, despite the

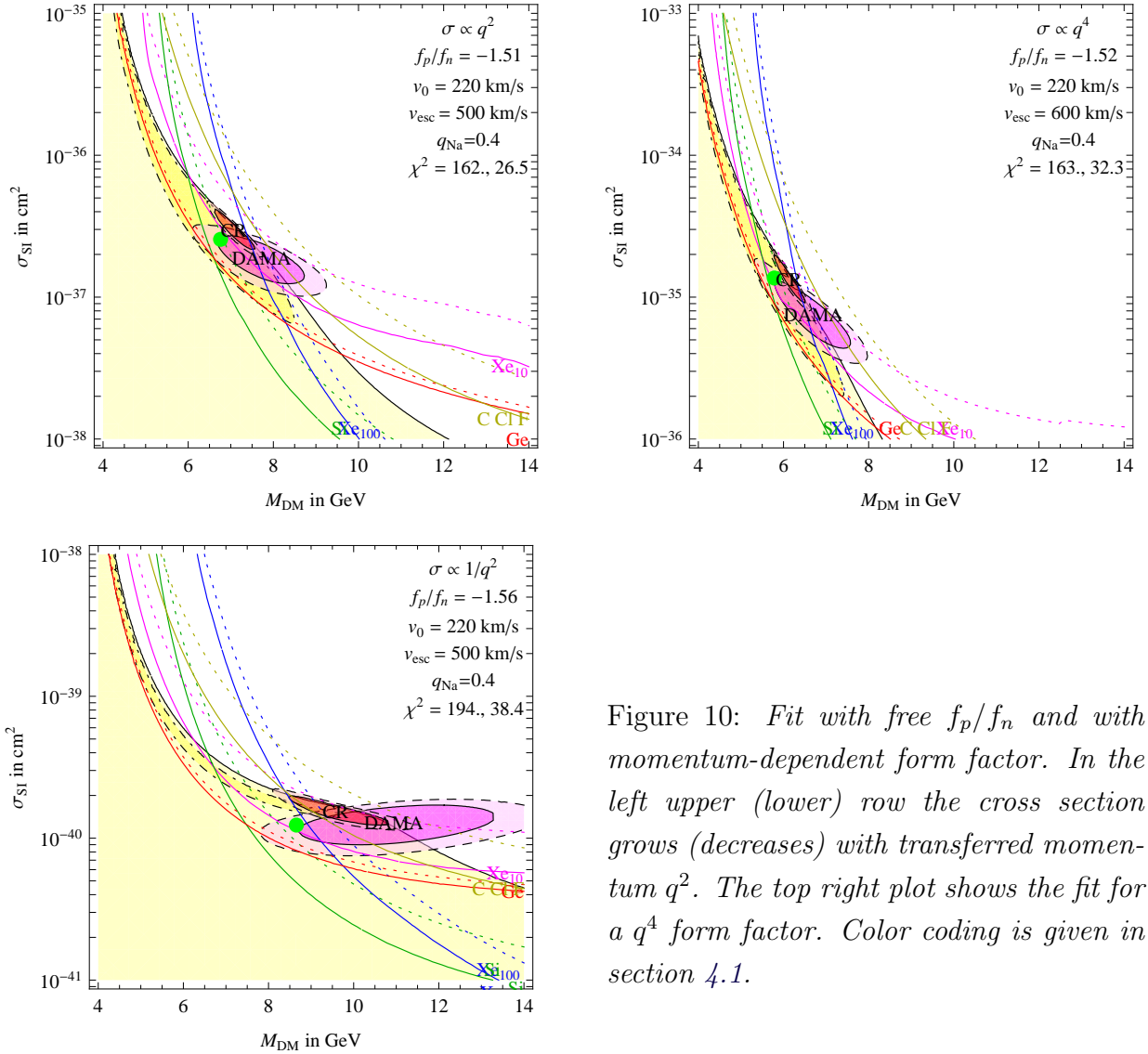


Figure 10: Fit with free f_p/f_n and with momentum-dependent form factor. In the left upper (lower) row the cross section grows (decreases) with transferred momentum q^2 . The top right plot shows the fit for a q^4 form factor. Color coding is given in section 4.1.

assumption of a relatively large Sodium quenching factor, $q_{Na} = 0.4$. Indeed, the incompatibility of the tentative DM signals is with four experiments, performed with three different nuclei (Xe, Si and Ge). Consequently, this extra parameter allows to avoid the strongest constraint (coming from Xe experiments), but is insufficient to relieve the tension completely.

4.6 Momentum-dependent elastic scattering

Momentum dependent scattering arise in several instances. One notable case is when the DM-nucleon interaction is mediated by a pseudo-scalar. It is possible to systematically study the momentum dependent effects by utilizing non-relativistic effective theory. Indeed, the typical energy transfer in DM-nucleus collisions relevant for direct-detection is much below the nuclear binding energy. Additionally, the DM velocity, $v \simeq 10^{-3}$, is non-relativistic. Consequently, it is possible to describe the scatterings via an effective theory assuming a rotationally invariant potential [57]. Restricting to spin-independent interactions, one finds to leading order in the

DM velocity, v , and the momentum transfer, q , only four scalar operators from which the effective potential may be constructed. Written in momentum space they are,

$$\begin{aligned}\mathcal{A}_1 &\propto 1, & \sigma &\propto 1, \\ \mathcal{A}_2 &\propto \vec{s}_{\text{DM}} \cdot \vec{q}, & \sigma &\propto q^2, \\ \mathcal{A}_3 &\propto \vec{s}_{\text{DM}} \cdot \vec{v}, & \sigma &\propto v^2, \\ \mathcal{A}_4 &\propto \vec{s} \cdot \vec{q} \times \vec{v}, & \sigma &\propto q^2 v^2,\end{aligned}\tag{4.1}$$

where \vec{s}_{DM} the spin of the DM. In a Lorentz invariant theory, specific linear combinations of the \mathcal{A} s appear in the full DM $N \rightarrow \text{DM } N$ amplitude. For further discussion, see [57].

From a phenomenological point of view we can study the effect of v - and q -dependent form factor on the compatibility between DAMA, CoGENT and the null-experiments. We consider the following DM form factors that enter in Eq. (2.2):

$$F_{\text{DM}}^2 = q^2/q_{\text{ref}}^2, \quad q^4/q_{\text{ref}}^4, \quad q_{\text{ref}}^2/q^2, \quad q_{\text{ref}}^4/q^4,\tag{4.2}$$

where the momentum transfer is normalized with respect to the reference $q_{\text{ref}} = 100 \text{ MeV}$. The last form factor can be generated in models where DM-nucleon scattering is mediated by a new particle with mass $m \ll q_{\text{ref}}$. The $1/q^2$ form factor can arise in this model with a coupling of type \mathcal{A}_2 .

A momentum-dependent form factor changes the relative rate in different experiments according to the range of q^2 they probe, as summarized in Fig. 9a. We show bands corresponding to the signal regions for DAMA (2-6 keVee) and for CoGENT (0.5-3 keVee), as well as lower q^2 value corresponding to the energy threshold for all other experiments. For SIMPLE we show the q^2 corresponding to fluorine which is target element with the largest rate thus being the main contributor to bounds.

q^2 and q^4 form factors help in this respect since they deplete the spectrum at low recoil energies and hence require smaller masses for a good fit. The XENON100 bounds are expected to get stronger relative to the other experiment due to the higher momentum transfer. It must be noted, however, that in the low mass region, the sensitivity of XENON100 is saturated by its threshold (and consequently the bound becomes vertical at small masses). Another feature of q^n ($n > 0$) form factors is that they enhance the CoGENT signal with respect to the DAMA one, since the former probes a higher q region. This implies that the ratio of the best-fit cross sections for CoGENT and DAMA will be smaller with respect to the standard fit, making the separation of the two regions more severe. This problem can be ameliorated by an appropriate choice of $f_n \neq f_p$. Fig. 10a shows the global fit. We find that q^2 form factor gives mildly better fits than the standard q^0 case, however the overall χ^2 remains poor. Similar results are found for a q^4 form factor.

An analog, but inverted, discussion apply for $1/q^2$ or $1/q^4$ form factors. These form factors move both the DAMA and CoGENT regions to higher masses and make the two best-fit points closer (assuming $f_n = f_p$). The DAMA non-modulated signal, which probes recoil energies below the ones where modulation is observed, excludes the q^{-4} behavior. Fig. 10b shows the results for $1/q^2$. We do not find that the form factor improves the global fit.

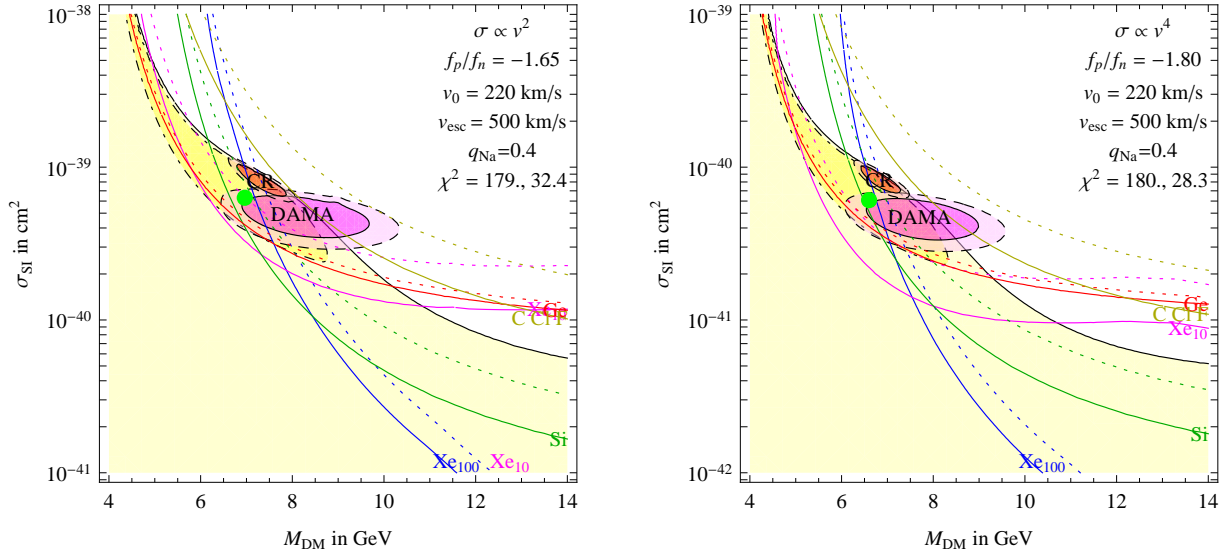


Figure 11: Fit with free f_p/f_n and with a velocity dependent form factor. **Left:** v^2 form factor. **Right:** v^4 form factor. An overall normalization effect is visible, as discussed in Section 2.1. For further discussion see Section 4.7. Color coding is given in section 4.1.

4.7 Velocity-dependent elastic scattering

The amplitudes in Eq. (4.1) also induce velocity-dependent form factors. Here we take again the phenomenological approach and study the effect of the form-factors,

$$F_{\text{DM}}^2 = v^2/v_0^2, \quad F_{\text{DM}}^2 = v^4/v_0^4, \quad (4.3)$$

where we normalize with respect to a mean velocity v_0 .

The effect of the overall normalization discussed in Section 2.1 and shown in Fig. 1 is trivial, as can be seen in the fits displayed in Fig. 11. To understand the effect of the sensitivity to the minimal velocity, we show the minimal DM velocity probed by different experiments as a function of the DM mass in Fig. 9b. We note that the minimal velocity does not depend on astrophysics (i.e. velocity distributions) nor on the scattering cross sections (see also [26]). The bands for COGENT and DAMA corresponding to the observed signal energy range are shown. For null-experiments we show the v_{min} corresponding to the respective energy threshold, where we have taken 3 keV as a representative value for XENON100. For completeness, the horizontal lines show the maximum velocity that a DM can have with respect to the Earth, given $v_{\text{esc}} = 500$ or 600 km/s . We see that neither COGENT nor DAMA probe values of v inaccessible to other experiments.

Nonetheless, some improvement in the global fit occurs when the typical minimal velocity is around the tail of the η_n function. In that region, a small change in sensitivity to v_{min} results in a large change in the scattering rate. Indeed our global fits shown in Fig. 11 demonstrate a small improvement in the fits.

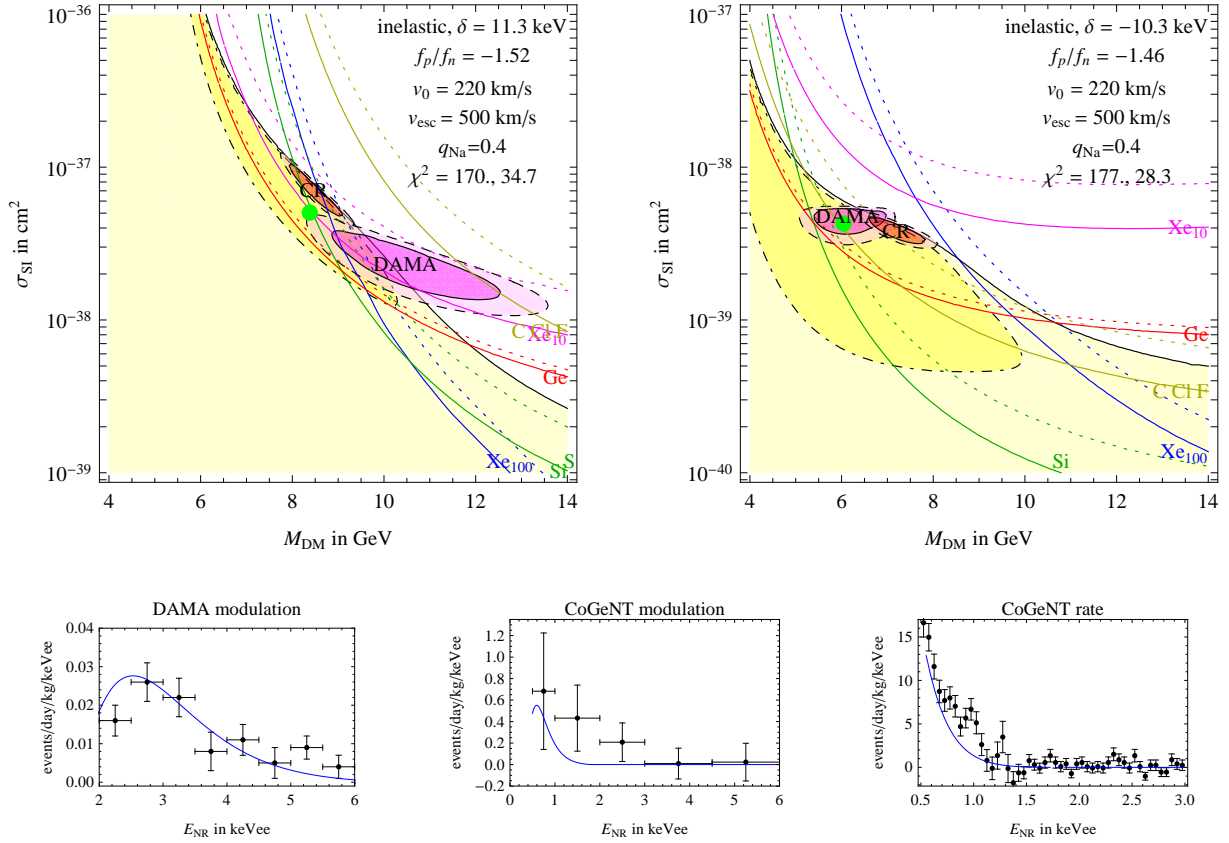


Figure 12: *Fit with inelastic dark matter and free f_p/f_n and DM splitting, δ . Left: An example of endothermic DM ($\delta > 0$), which improve the global fit. Right: exothermic DM ($\delta < 0$) improves the partial fit. Color coding is described in Section 4.1. Bottom: DM predictions at the best fit point in the right panel (exothermic DM), plotted against the DAMA and CoGeNT modulated and unmodulated data.*

4.8 Inelastic light Dark Matter scattering

It is possible that DM scatters inelastically with the nucleus. For inelastic scattering to take place, two semi-degenerate DM states are assumed, with mass splitting $\delta = M'_{\text{DM}} - M_{\text{DM}}$. Up-scattering of the lighter DM state requires it to have enough energy, thereby suppressing the rate for small values of the recoil energy. Since up-scattered iDM kinematically favors heavy targets, it was originally able to ameliorate the tension between the DAMA modulation and the null CDMS result [9], requiring $M_{\text{DM}} \sim 100$ GeV and $\delta \sim 100$ keV.

This original iDM scenario seems now excluded by the recent XENON100 results [58, 59]. Here we study a different iDM regime with significantly smaller splitting and lighter DM (for previous study see [15]). In this window the tension with the null experiments is ameliorated mostly due to the small DM mass, while the DM scattering rate is falling above a few keV, much like in the elastic case. The effect of δ , is to modify the minimal velocity needed for scattering to occur, in accord with Eq. (2.4).

For the masses and recoil energies of interest, the splitting δ is required to be smaller than ~ 15 keV in order to comply with the COGENT data. Consequently, the inelasticity for up-scattering is only relevant for the light Sodium and Silicon targets in DAMA and CDMS respectively. We find that such scenario does improve the global fit only slightly, and one example for $\delta \approx 11$ keV is shown in Fig. 12a

It is possible, however, that the heavier DM state is cosmologically long lived, in which case it occupies a sizable fraction of the DM density. In fact, this possibility occurs quite naturally, as noted in [60, 61]. In such a case, DM can also down-scatter with the nucleus, producing an exothermic reaction. This possibility, dubbed exoDM (exoDM), was studied in [61]. Technically, the rate for exoDM is given by the same expression as for the up-scattered iDM case, with now $\delta < 0$. But the behavior of exoDM is significantly different. The minimal velocity, Eq. (2.4), is minimized for $E_R \simeq |\delta|\mu/m_N$ and hence lighter targets are more sensitive to exothermic DM scatterings. No net modulation in the total number of signal events is expected. However, since the spread of the spectrum around its maximum depends on the DM kinetic energy, the recoil energy spectrum will actually modulate annually. The modulated spectrum observed by DAMA can thus be reproduced [61].

In Fig. 12b we show the best fit for exoDM. In order to isolate the effect of down-scattering, here we only consider down-scattered events, even though up-scattering is expected to be significant. For the fit, we float the DM mass, the cross section, f_p/f_n and the DM mass splitting, finding that a $\delta \approx -10$ keV improves the partial fit with respect to the analogous fit with $\delta = 0$, shown in Fig. 8b.

4.9 Channeling

We now allow for some amount of channeling in the NaI(Tl) crystals of DAMA and/or in COGENT. In this section we do not introduce any inelasticity: $\delta = 0$. Fig. 13a shows how a relatively small fraction of channeled events is enough to shift the best fit regions for these experiments to a different global minimum of the χ^2 . Next, increasing the channeling fraction further, mildly shifts the best-fit regions down to lower values of the cross section, but no new best-fit regions appear. The effect of channeling can easily be understood:

- In COGENT, the channeled best-fit region has a DM mass reduced by a factor ≈ 0.5 (the square root of the quenching factor in eq. (3.5)).
- In DAMA, scattering on lighter Na (on heavier Iodine) dominates if channeling is negligible (significant), and the best-fit region almost corresponds to the same DM mass, as shown in Fig. 13a.

Adding channeling only in DAMA allows to get a best fit comparable to the un-channeled best fit. Fig. 13b shows one example of this possibility, assuming a 10% channeling in DAMA.

Adding channeling also in COGENT moves its best fit to a smaller DM mass. Interestingly, with little channeling, no inelasticity and no isospin-violating interactions, we obtain an

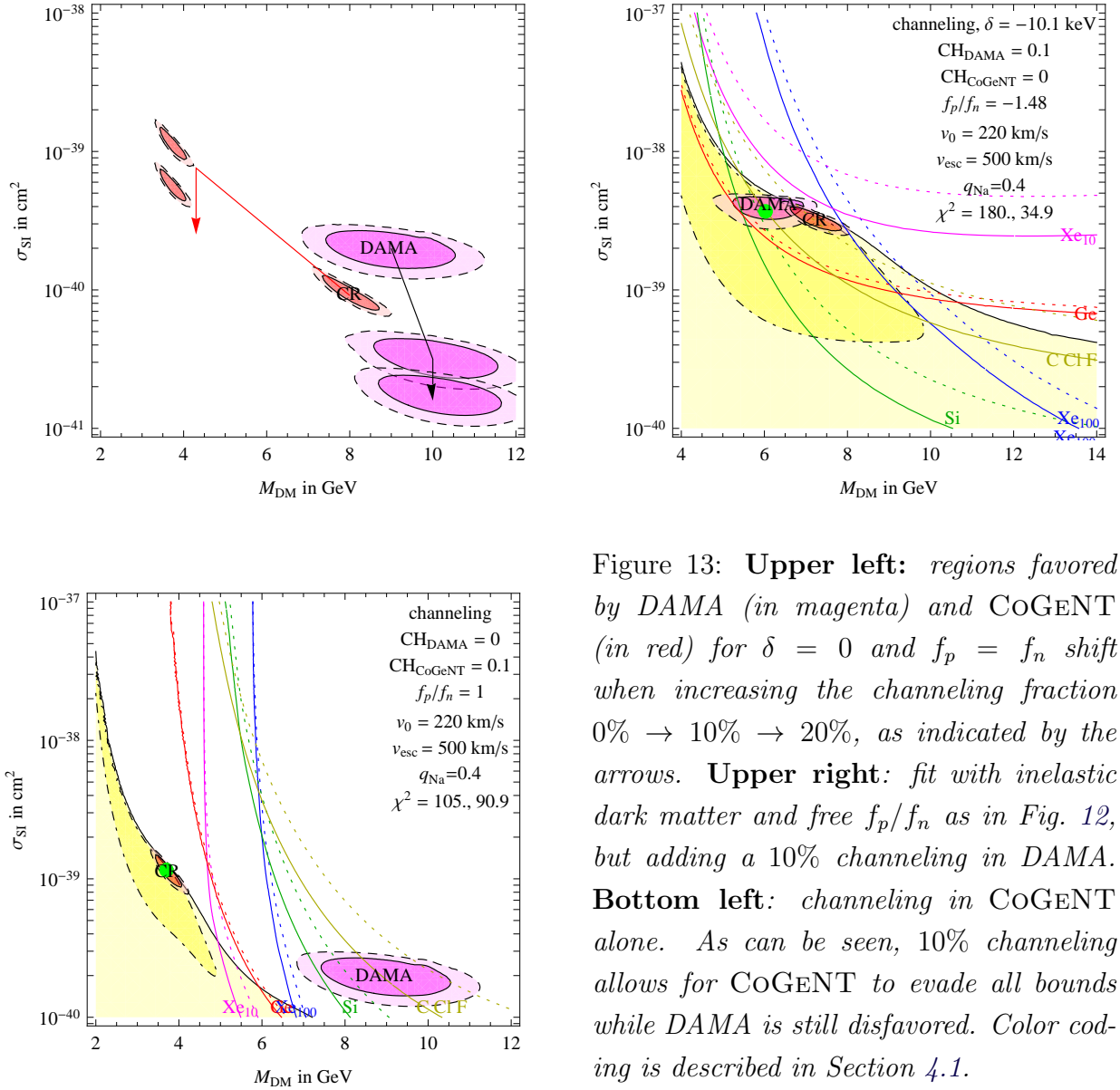


Figure 13: **Upper left:** regions favored by DAMA (in magenta) and COGENT (in red) for $\delta = 0$ and $f_p = f_n$ shift when increasing the channeling fraction $0\% \rightarrow 10\% \rightarrow 20\%$, as indicated by the arrows. **Upper right:** fit with inelastic dark matter and free f_p/f_n as in Fig. 12, but adding a 10% channeling in DAMA. **Bottom left:** channeling in COGENT alone. As can be seen, 10% channeling allows for COGENT to evade all bounds while DAMA is still disfavored. Color coding is described in Section 4.1.

improved best fit ($\chi^2 \sim 100$), corresponding to fitting COGENT compatibly with null experiments, but at the price of giving almost no signal in DAMA, which prefers a higher DM mass. We plot this possibility in Fig. 13c.

4.10 Channeling plus inelasticity

The incompatibility between the channeled DAMA and COGENT best fits in Fig. 13a or c, where we assumed $f_p/f_n = 1$ and $\delta = 0$, can be eliminated varying these two parameters. Two kind of best fits appear:

- The ‘usual’ best fit at higher $M_{\text{DM}} \approx 6$ GeV, with a slightly improved χ^2 , as shown in Fig. 14a.

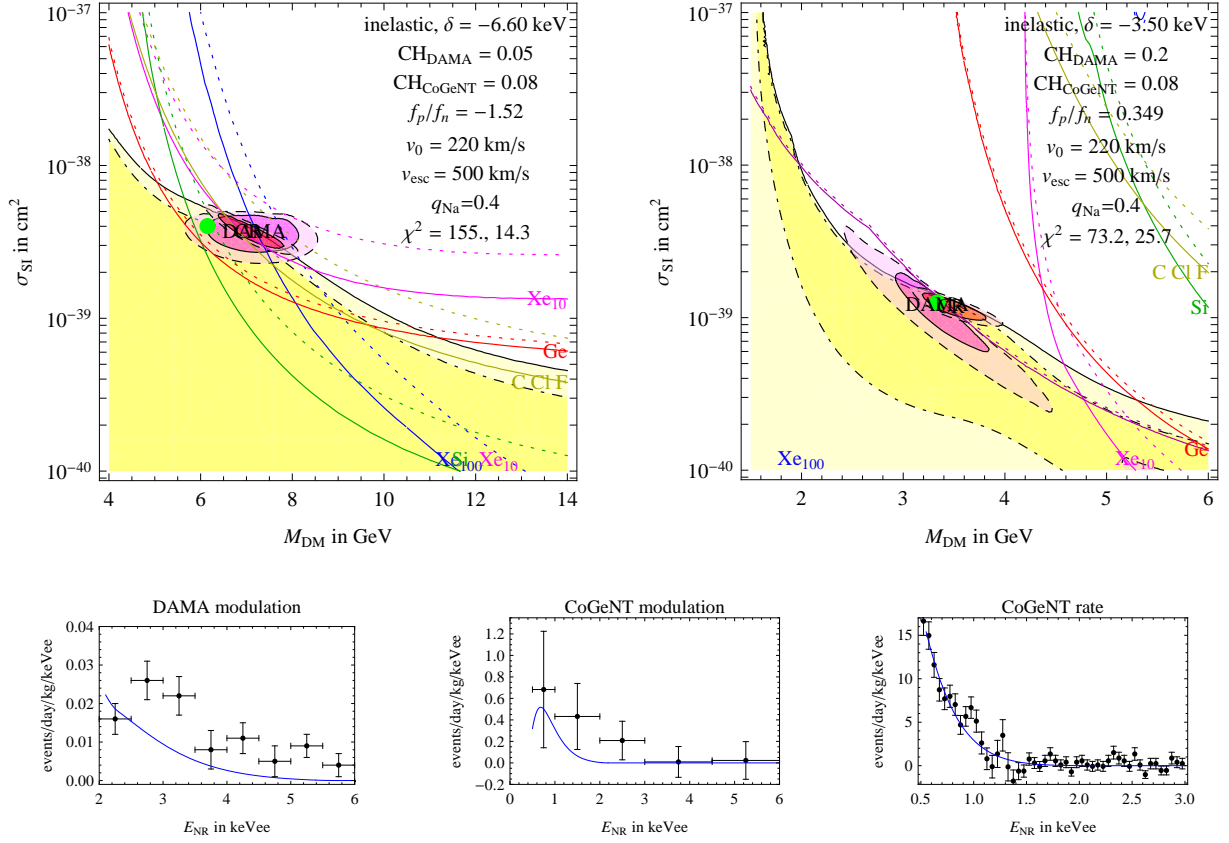


Figure 14: *Fit with channeling in both DAMA and CoGENT together with inelasticity. Left: global best fit at larger mass. Right: new best fit at smaller mass as discussed in Section 4.10. The dark magenta line is the bound from DAMA unmodulated signal. Bottom: DM predictions at the best fit point in the right panel.*

- A new kind of best fit, shown in Fig. 14b, that makes use of the channeled CoGENT best fit at smaller $M_{DM} \approx 3$ GeV, and that employs inelasticity and channeling to also shift the DAMA best fit region to such a small mass. Indeed, a new local minimum of the DAMA-only fit appears at small mass for large enough channeling in DAMA. In Fig. 14b we assumed a 20% channeling fraction, that is enough to have both DAMA best fits with comparable χ^2 . We find the exoDM (shown in the figure) to have a better global fit, however under the assumptions above, a lower mass region exists for endothermic DM too.

The quality of the new best fit is now very significantly improved. It makes use of channeling only in DAMA and CoGENT, of inelasticity and of isospin violation. It relies on channeled sodium events to constitute the bulk of the DAMA signal.

Due to the small fractional modulation (the ratio between the modulated and unmodulated signal) characteristic of exothermic DM, non trivial bounds on this region come from demanding that the DM rate does not exceed the total rate measured by DAMA, in particular in the 1-2

keVee range. The dark magenta curve in Fig. 14b shows such bound. This constraint becomes less stringent for smaller values of $|\delta|$ (which worsen the fit) or under the assumption that the channeling fraction drops at energies below ~ 2 keVee.

5 Conclusions

We explored the prospects of dark matter for jointly explaining the modulations signals observed by DAMA and CoGENT while complying with the constraints from other direct detection experiments: XENON10, XENON100, CDMS-Ge, CDMS-Si and SIMPLE. In the minimal scenario of spin-independent isospin-symmetric scattering there is a clear incompatibility, if we adhere to the data analyses performed by the experimental collaborations. Taking into account uncertainties on the astrophysical velocity distribution of DM and allowing for a higher sodium quenching factor in DAMA, $q_{\text{Na}} = 0.4$ does not significantly improve the fits. Furthermore, DAMA and CoGENT are mutually incompatible.

Assuming different DM cross sections on proton and neutrons allows to significantly improve the situation, making DAMA and CoGENT compatible and weakening one of the bounds from the null experiments. The best fit is for $f_p/f_n \approx -1.5$, which allows to weaken the dominant bounds from experiments with Xenon. However the overall global fit remains poor, see Fig. 8. Some additional improvement (although not very significant) is obtained by allowing for a DM/nucleon form factor that depends on the transferred momentum and/or on the relative velocity. A similar results holds for inelastic scattering of DM with a mass splitting, $\delta = M'_{\text{DM}} - M_{\text{DM}}$. Both up-scattering ($\delta > 0$) and down-scattering ($\delta < 0$) were considered. The best global fit to all relevant experiments is obtained as in Fig. 12 for $|\delta| \approx 10$ keV.

A modest channeling in DAMA allows a further slight improvement. Allowing also for a $\sim 10\%$ channeling in CoGENT results in a fit at smaller $M_{\text{DM}} \approx 3$ GeV, that, together with a $\sim 20\%$ channeling in DAMA and inelasticity, allows a good global fit (Fig. 14b).

We stress the alternative simple possibility of mild channeling in CoGENT alone: it allows for a good CoGENT fit (without assuming a tuned inelasticity nor isospin-violating interactions) but excludes the DAMA signal.

In conclusion, we find it hard to explain the full set of current direct detection experiments with spin-independent scattering of dark matter, and contemplate on the possibility that one or both of the positive signals does not arise from DM interactions.

Note added: While this work was being finalized, related works appeared [62, 63].

Acknowledgements We thank Juan Collar, Mariangela Lisanti, Jeremy Mardon and Tracy Slatyer for useful discussions. We wish to thank the authors of [64] for pointing out an error in Section 3.2 in an earlier version of the paper. The work of AS was supported by the ESF grant MTT8 and by SF0690030s09 project. The work of DP was supported by the Swiss National Science Foundation under contract No. 200021-116372. The work of MF was supported in part

by the European Programme “Unification in the LHC Era”, contract PITN-GA-2009-237920 (UNILHC). The work of TV was supported in part by the Director, Office of Science, Office of High Energy and Nuclear Physics, of the US Department of Energy under Contract DE-AC02-05CH11231. AS thanks the invitation from the Berkeley physics department, where this work was initiated. This work was supported by the EU ITN Unification in the LHC Era, contract PITN- GA-2009-237920 (UNILHC).

References

- [1] DAMA collaboration, Eur. Phys. J. C56 (2008) 333 [arXiv:0804.2741].
- [2] CoGENT collaboration, [arXiv:1002.4703].
- [3] C. E. Aalseth *et al.*, [arXiv:1106.0650].
- [4] CDMS-II collaboration, Science 327 (2010) 1619-1621 [arXiv:0912.3592].
- [5] XENON10 collaboration, Phys. Rev. D 80, 115005 (2009) [arXiv:0910.3698].
- [6] XENON100 collaboration, [arXiv:1104.2549].
- [7] J. Kopp, V. Niro, T. Schwetz and J. Zupan, Phys. Rev. D 80, 083502 (2009) [arXiv:0907.3159].
- [8] B. Feldstein, P. W. Graham and S. Rajendran, Phys. Rev. D 82, 075019 (2010) [arXiv:1008.1988].
- [9] D. Tucker-Smith and N. Weiner, Phys. Rev. D 64, 043502 (2001) [arXiv:hep-ph/0101138].
- [10] P. W. Graham, R. Harnik, S. Rajendran and P. Saraswat, Phys. Rev. D 82, 063512 (2010) [arXiv:1004.0937].
- [11] J. M. Cline, A. R. Frey, F. Chen, Phys. Rev. D83, 083511 (2011). [arXiv:1008.1784].
- [12] A. Kurylov and M. Kamionkowski, Phys. Rev. D 69, 063503 (2004) [arXiv:hep-ph/0307185].
- [13] F. Giuliani, Phys. Rev. Lett. 95, 101301 (2005) [arXiv:hep-ph/0504157].
- [14] R. C. Cotta, J. S. Gainer, J. L. Hewett and T. G. Rizzo, New J. Phys. 11, 105026 (2009) [arXiv:0903.4409].
- [15] S. Chang, J. Liu, A. Pierce, N. Weiner and I. Yavin, JCAP 1008, 018 (2010) [arXiv:1004.0697].
- [16] Z. Kang, T. Li, T. Liu, C. Tong and J. M. Yang, JCAP 1101, 028 (2011) [arXiv:1008.5243].
- [17] J. L. Feng, J. Kumar, D. Marfatia and D. Sanford, [arXiv:1102.4331].
- [18] E. Del Nobile, C. Kouvaris and F. Sannino, [arXiv:1105.5431].
- [19] B. Feldstein, A. L. Fitzpatrick and E. Katz, JCAP 1001, 020 (2010) [arXiv:0908.2991].
- [20] S. Chang, A. Pierce and N. Weiner, JCAP 1001, 006 (2010) [arXiv:0908.3192].
- [21] Y. Bai and P. J. Fox, JHEP 0911, 052 (2009) [arXiv:0909.2900].
- [22] M. C. Smith *et al.*, Mon. Not. Roy. Astron. Soc. 379, 755 (2007) [arXiv:astro-ph/0611671].
- [23] T. Bruch, J. Read, L. Baudis and G. Lake, Astrophys. J. 696 (2009) 920 [arXiv:0804.2896]; D. Stiff, L. M. Widrow and J. Frieman, Phys. Rev. D 64 (2001) 083516 [arXiv:astro-ph/0106048]; K. Freese, P. Gondolo, H. J. Newberg and M. Lewis, Phys. Rev. Lett. 92 (2004) 111301 [arXiv:astro-ph/0310334]; P. Gondolo and G. Gelmini, Phys. Rev. D 71 (2005) 123520 [arXiv:hep-ph/0504010]; J. March-Russell, C. McCabe and M. McCullough, JHEP 0905 (2009) 071 [arXiv:0812.1931]; F. S. Ling, Phys. Rev. D 82 (2010) 023534 [arXiv:0911.2321]; R. F. Lang and N. Weiner, JCAP 1006 (2010) 032 [arXiv:1003.3664]; C. McCabe, Phys. Rev. D 82 (2010) 023530 [arXiv:1005.0579]; A. M. Green, JCAP 1010 (2010) 034 [arXiv:1009.0916]; M. Lisanti and D. N. Spergel, [arXiv:1105.4166].

- [24] M. Fairbairn and T. Schwetz, JCAP 0901, 037 (2009) [arXiv:[0808.0704](#)].
- [25] M. Kuhlen *et al.*, JCAP 1002, 030 (2010) [arXiv:[0912.2358](#)].
- [26] P. J. Fox, J. Liu and N. Weiner, Phys. Rev. D 83, 103514 (2011) [arXiv:[1011.1915](#)].
- [27] P. J. Fox, G. D. Kribs and T. M. P. Tait, Phys. Rev. D 83 (2011) 034007 [arXiv:[1011.1910](#)].
- [28] C. Savage, K. Freese and P. Gondolo, Phys. Rev. D 74 (2006) 043531 [arXiv:[astro-ph/0607121](#)].
- [29] M. Lisanti, L. E. Strigari, J. G. Wacker and R. H. Wechsler, Phys. Rev. D 83, 023519 (2011) [arXiv:[1010.4300](#)].
- [30] C. Arina, J. Hamann and Y. Y. Y. Wong, [arXiv:[1105.5121](#)].
- [31] E. M. Drobyshevski, Mod. Phys. Lett. A 23 (2008) 3077 [arXiv:[0706.3095](#)].
- [32] R. Bernabei *et al.*, Eur. Phys. J. C 53 (2008) 205 [arXiv:[0710.0288](#)].
- [33] N. Bozorgnia, G. B. Gelmini and P. Gondolo, JCAP 1011, 019 (2010) [arXiv:[1006.3110](#)]. N. Bozorgnia, G. B. Gelmini and P. Gondolo, JCAP 1011, 028 (2010) [arXiv:[1008.3676](#)]. N. Bozorgnia, G. B. Gelmini and P. Gondolo, JCAP 1011, 029 (2010) [arXiv:[1009.3325](#)].
- [34] J. I. Collar, [arXiv:[1106.0653](#)].
- [35] D. Hooper and C. Kelso, [arXiv:[1106.1066](#)]; M. T. Frandsen, F. Kahlhoefer, J. March-Russell, C. McCabe, M. McCullough and K. Schmidt-Hoberg, [arXiv:[1105.3734](#)].
- [36] J. D. Lewin and P. F. Smith, Astropart. Phys. 6 (1996) 87.
- [37] M. Vogelsberger *et al.*, [arXiv:[0812.0362](#)].
- [38] F. S. Ling, E. Nezri, E. Athanassoula and R. Teyssier, JCAP 1002, 012 (2010) [arXiv:[0909.2028](#)].
- [39] D. R. Tovey, V. Kudryavtsev, M. Lehner *et al.*, Phys. Lett. B433, 150-155 (1998).
- [40] H. Chagani, P. Majewski, E. J. Daw *et al.*, JINST 3, P06003 (2008). [arXiv:[0806.1916](#)].
- [41] DAMA collaboration, Eur. Phys. J. C 56, 333 (2008) [arXiv: [0804.2741](#)].
- [42] M. Papucci and A. Strumia, JCAP 1003 (2010) 014 [arXiv:[0912.0742](#)].
- [43] J. Collar, *Private communication*.
- [44] M. Felizardo *et al.*, [arXiv:[1106.3014](#)].
- [45] G. Plante *et al.*, [arXiv:[1104.2587](#)].
- [46] C. Savage, G. Gelmini, P. Gondolo, K. Freese, Phys. Rev. D83, 055002 (2011). [arXiv:[1006.0972](#)].
- [47] XENON100 collaboration, [arXiv:[1103.0303](#)].
- [48] XENON10 collaboration, [arXiv:[1104.3088](#)].
- [49] A. Manzur, A. Curioni, L. Kastens, D. N. McKinsey, K. Ni and T. Wongjirad, Phys. Rev. C 81, 025808 (2010) [arXiv:[0909.1063](#)].
- [50] M. Horn *et al.*, [arXiv:[1106.0694](#)].
- [51] S. Yellin, Phys. Rev. D 66, 032005 (2002) [arXiv:[physics/0203002](#)].
- [52] J. Filippini, PhD Thesis, University of California at Berkeley (2008).
- [53] J. Filippini [CDMS Collaboration], *Les Rencontres de Physique de la Vallée d'Aoste*, Nuovo Cimento C 32 05-06 (2009).

- [54] D. Hooper, J. I. Collar, J. Hall, D. McKinsey, Phys. Rev. D82, 123509 (2010). [arXiv:[1007.1005](#)].
- [55] CDMS-II collaboration, Phys. Rev. Lett. 106, 131302 (2011) [arXiv:[1011.2482](#)].
- [56] J. I. Collar, [arXiv:[1103.3481](#)].
- [57] J. Fan, M. Reece and L. T. Wang, JCAP 1011 (2010) 042 [arXiv:[1008.1591](#)].
- [58] XENON100 collaboration, [arXiv:[1104.3121](#)].
- [59] M. Farina, M. Kadastik, D. Pappadopulo, J. Pata, M. Raidal and A. Strumia, [arXiv:[1104.3572](#)].
- [60] D. P. Finkbeiner, T. R. Slatyer, N. Weiner and I. Yavin, JCAP 0909 (2009) 037 [arXiv:[0903.1037](#)]; B. Batell, M. Pospelov and A. Ritz, Phys. Rev. D 79 (2009) 115019 [arXiv:[0903.3396](#)].
- [61] R. Essig, J. Kaplan, P. Schuster and N. Toro, [arXiv:[1004.0691](#)]; “Exothermic Dark Matter,” Phys. Rev. D 82 (2010) 063512 [arXiv:[1004.0937](#)].
- [62] P. Belli, R. Bernabei, A. Bottino, F. Cappella, R. Cerulli, N. Fornengo and S. Scopel, [arXiv:[1106.4667](#)]
- [63] T. Schwetz and J. Zupan, [arXiv:[1106.6241](#)]
- [64] P. J. Fox, J. Kopp, M. Lisanti, N. Weiner, [arXiv:[1107.0717](#)].